

REPORT DOCUMENTATION PAGE

Form Approved
OMB No. 0704-0188

Public reporting burden for this collection of information is estimated to average 1 hour per response, including the time for reviewing instructions, searching existing data sources, gathering and maintaining the data needed, and completing and reviewing this collection of information. Send comments regarding this burden estimate or any other aspect of this collection of information, including suggestions for reducing this burden to Department of Defense, Washington Headquarters Services, Directorate for Information Operations and Reports (0704-0188), 1215 Jefferson Davis Highway, Suite 1204, Arlington, VA 22202-4302. Respondents should be aware that notwithstanding any other provision of law, no person shall be subject to any penalty for failing to comply with a collection of information if it does not display a currently valid OMB control number. **PLEASE DO NOT RETURN YOUR FORM TO THE ABOVE ADDRESS.**

1. REPORT DATE (DD-MM-YYYY)		2. REPORT TYPE	3. DATES COVERED (From - To)		
4. TITLE AND SUBTITLE			5a. CONTRACT NUMBER		
			5b. GRANT NUMBER		
			5c. PROGRAM ELEMENT NUMBER		
6. AUTHOR(S)			5d. PROJECT NUMBER		
			5e. TASK NUMBER		
			5f. WORK UNIT NUMBER		
7. PERFORMING ORGANIZATION NAME(S) AND ADDRESS(ES)			8. PERFORMING ORGANIZATION REPORT NUMBER		
9. SPONSORING / MONITORING AGENCY NAME(S) AND ADDRESS(ES)			10. SPONSOR/MONITOR'S ACRONYM(S)		
			11. SPONSOR/MONITOR'S REPORT NUMBER(S)		
12. DISTRIBUTION / AVAILABILITY STATEMENT					
13. SUPPLEMENTARY NOTES					
14. ABSTRACT					
15. SUBJECT TERMS					
16. SECURITY CLASSIFICATION OF:			17. LIMITATION OF ABSTRACT	18. NUMBER OF PAGES	19a. NAME OF RESPONSIBLE PERSON
a. REPORT	b. ABSTRACT	c. THIS PAGE			19b. TELEPHONE NUMBER (include area code)

Type II Superlattice as Low-Temperature Peltier Refrigerator (4 K - 150 K) Final Report

PI: Matthew Grayson
Assistant Professor
Electrical Engineering and Computer Science
Northwestern University

Collaborators:

Northwestern University
Electrical Engineering and Computer Science

Faculty: Prof. Seda Memik
Doctoral Students: Chuanle Zhou, Jieyi Long, Yang Tang
Masters Students: Andrew Varrenti, Rebecca Seung Chyung
Undergraduates: Andrea Grace Klock, Marissa Norko, Karen Heinselman, Rebecca Seung Chyung

Technische Universitaet Muenchen
Walter Schottky Institut

Faculty: Prof. Gerhard Abstreiter, Dr. Gregor KoblmueLLer
Doctoral Students: Stefan Birner

Preprints:

JOURNAL ARTICLES:

- 1) A. R. Varrenti, Chuanle Zhou, A. G. Klock, S. H. Chyung, J. Long, S. O. Memik, M. Grayson, "Thermal sensing with lithographically patterned bimetallic thin-film thermocouples," IEEE Electron Device Letters 32, 818 (2011).
- 2) Chuanle Zhou, B.-M. Nguyen, M. Razeghi, and M. Grayson, "Thermal conductivity of InAs/GaSb superlattice," accepted to Journal of Electronic Materials, 29 Feb (2011).

CONFERENCE PROCEEDINGS:

- 3) C. Zhou, M. Norko, Y. Tang, and M. Grayson, "InAs/GaSb Type II Superlattices as Low-Temperature Thermoelectrics," 15th International Conference on Narrow Gap Systems (NGS15), AIP Conf. Proc. 1416, 142 (2011).
- 4) Jieyi Long, A. G. Klock, Chuanle Zhou, Seda Ogrenci Memik, M. Grayson, "IOTA: Towards an integrated on-chip thermocouple array," 16th International Workshop on Thermal Investigations of ICs and Systems (THERMINIC), 1-6 (2010).
- 5) Jieyi Long, S. O. Memik, M. Grayson, "Optimization of an on-chip active cooling system based on thin-film thermoelectric coolers," Design, Automation & Test in Europe Conference & Exhibition (DATE), 117 (2010).

PATENTS:

- 6) M. Grayson, C. Zhou, A. Klock, S. Memik, Jieyi Long, Patent Application, Utility Filing Serial # 12/924,091, "On-chip thermocouple array," 2010.
- 7) M. Grayson, C. Zhou, "Transverse thermoelectrics," Patent Pending, (submitted 2011).

Service and Organization:

Assisted in organizing speakers for workshop on low-temperature Peltier cooling,
Albuquerque, NM, April 22-23, 2009

Invited guests:

Prof. Peter Vogl from Technische Universitaet Muenchen, Munich, Germany

Prof. Francesco Giazzotto from Scuola Normale, Pisa, Italy

Dr. Niels Oeschler from Max-Planck-Institut, Dresden, Germany

Dr. Simon Johnsen from Max-Planck-Institut, Dresden, Germany,

Equipment Purchased/Designed/Installed:

Oxford VTI Probe, with 24 coaxial cable leads for high impedance measurements up to 100
G Ω

Custom designed copper block mount for sample probe

Custom modified DIP-headers for sample mounting with accurate thermometry

Test calibration of thermometry from 300 K to 1.5 K

Test sweep of magnetic field from 0 to 17 T

Custom designed rapid thermal annealer for ohmic contact diffusion

Report on Final Results

The Final Report is based around the central task put forth in the original proposal: to *theoretically estimate and optimize the figure of merit ZT for the type II superlattice (T2SL)*, and estimate whether it might work as a cryogenic Peltier cooler. This theoretical task required knowing all constituent parameters of the ZT coefficient, namely the Seebeck coefficient S , the electrical conductivity σ , and the thermal conductivity κ . In the process of developing the theory of the Seebeck coefficient for this material, a new transverse thermoelectric phenomenon at zero magnetic field was discovered which we call “anisotropic ambipolar transverse thermoelectrics” (AATT). This discovery required deeper theoretical understanding of transverse thermoelectric phenomena in general, with the accompanying realization that now 6 transport coefficients would be required to characterize this material: S_{xx} , S_{yy} , κ_{xx} , κ_{yy} , and ρ_{xx} , ρ_{yy} , where the resistivity tensor ρ is the inverse of the conductivity tensor. It was determined that S and ρ tensors could be calculated theoretically, but κ would have to be measured experimentally, and that the single component κ_{yy} would be sufficient to estimate device performance. In the end, the AATT behavior of the T2SL was determined to give a transverse $Z_{\perp}T = 0.026$ at room temperature which is able to produce 8 K of thermal cooling in exponentially tapered 10 micron thick films, and can yield a new microscale geometry for infrared pixel cooling. It was also determined that wide superlattice thicknesses which have a topological-insulator-like crossing of conduction and valence bands should provide greater $Z_{\perp}T$ values at cryogenic temperatures.

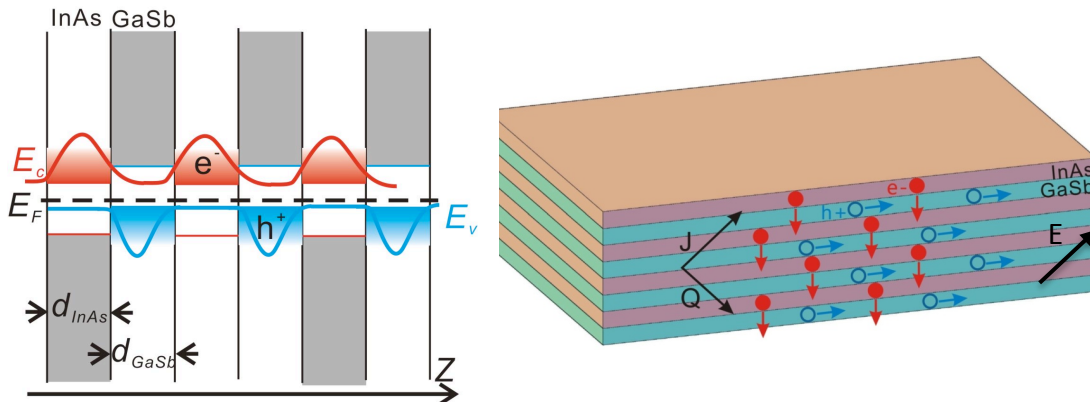


FIGURE OF TYPE II SUPERLATTICE: (left) Band-diagram illustration of type II superlattice of InAs (hosting electrons) and GaSb (hosting holes). Note that the heavy-mass holes are confined to their layer, whereas the light-mass electrons can freely tunnel between layers. Proper choice of chemical potential leads to a semiconductor with net n-type conduction out-of-plane and net p-type conduction in-plane. (right) Note that in the presence of a diagonal electric field E at 45 degrees, the net charge current will flow parallel to the electric field, yet the net particle current which carries heat will flow orthogonal to the electric field.

The remainder of this Final Report is therefore broken down in terms of five principle tasks:

- I. Description of the new transport equations of AATT materials
- II. Experimental determination of κ_{yy}
- III. Theoretical determination of S and ρ tensors for a given lattice period
- IV. Optimization of transverse figure of merit $Z_{\perp}T$ over all lattice periods with a description of a new device geometries
- V. Description of thin-metal-film thermocouple technology needed to characterize thermoelectric properties of T2SL films in the future

I. Transport equations for a new thermoelectric phenomenon: Ambipolar Anisotropic Transverse Thermoelectricity (AATT)

In spite of the prominent success of standard longitudinal thermoelectrics, there remain regimes of operation for which less conventional transverse thermoelectrics may prove advantageous. Longitudinal thermoelectrics are extrinsically doped p- or n-type with heat flow parallel or anti-parallel to the electrical current, respectively, optimized according to the figure of merit $ZT = S_{xx}^2 T / \rho_{xx} \kappa_{xx}$, with most recent progress above room temperature using nanoscale phonon scatters to limit the thermal conductivity κ_{xx} , while maintaining low electrical resistivity ρ_{xx} and large Seebeck coefficient S_{xx} . Transverse thermoelectrics, on the other hand, have a large off-diagonal component S_{xy} in the Seebeck tensor which causes heat to flow orthogonal to the electrical current with transverse figure of merit $Z_{\perp} T = S_{xy}^2 T / \rho_{xx} \kappa_{yy}$. Whereas the use of longitudinal thermoelectrics at low temperatures is restricted since the dopants freeze out at cryogenic temperatures, transverse thermoelectric phenomena are intrinsic since both electrons and holes transport heat so there is no dopant freeze-out. And whereas the minimum temperature for multistage longitudinal Peltier coolers is limited by electrical and thermal contact resistances at each stage, for transverse thermoelectrics the heat and electrical current flow cross-sections are orthogonal, and exponentially tapered devices function as infinite-stage Peltier refrigerators, predicted to cool to arbitrarily low temperatures.[¹] Regarding device scaling, the fabrication of microscale longitudinal thermoelectric devices can be quite challenging.[²] On the other hand, transverse thermoelectrics require only a single thermoelectric layer, so devices can be fabricated down to the nanoscale. Finally, with longitudinal thermoelectrics both p- and n-doped materials need to be separately optimized, but with transverse thermoelectrics, only one material solution is required.

In transverse thermoelectric phenomena the directional symmetry of the Seebeck tensor needs to be broken. Thermomagnetic effects such as the Ettingshausen effect require an external magnetic field to break the time-reversal symmetry thereby introducing off-diagonal terms in the Seebeck tensor and generating transverse heat flow.³ Composite transverse thermoelectrics have also been proposed which have a structural asymmetry imposed by stacking macroscopic millimeter-sized slabs,⁴ alternating a semiconductor with large Seebeck coefficient and a (semi)metal with large electrical and thermal conductivity. This composite can induce transverse heat flow when the current is skewed with respect to the layers. However, the usage of a high magnet field of 1.5 T in the former case limits the practical application of the Ettingshausen effect, and the stacking of macroscopic millimeter-scale slabs in the latter case does not permit small scale, compact devices.

This Final Report describes the band-engineering strategy which we call anisotropic ambipolar transverse thermoelectrics (AATT), whereby the anisotropic electron and hole mass tensors of a narrow gap superlattice result in orthogonal electron and hole currents and a large transverse Seebeck coefficient. The general requisite properties for AATT are outlined. Transport equations based on an electron-hole two-band model define the optimal angle of electric current for inducing the maximum transverse figure of merit $Z_{\perp} T$. The concept of a crossover electric field E_c in exponentially tapered devices is introduced and shown to distinguish thin and thick samples. The equations for thermoelectric transport in an exponentially tapered cooler are also explored, which in theory can yield an arbitrarily low cooling temperature with sufficiently thick layers allowing even poor $Z_{\perp} T$ materials to induce large thermal differences.

We begin with a study of how anisotropic electron and hole two-band conduction can lead to the

desired Seebeck anisotropy: an ambipolar Seebeck tensor which is n-type in one direction and p-type perpendicular. Consider the general case of a semiconductor near intrinsic doping with anisotropic electron and hole conductivity tensors $\boldsymbol{\sigma}_n$, $\boldsymbol{\sigma}_p$ and isotropic Seebeck tensors \mathbf{s}_n , \mathbf{s}_p where x and y axes align with the principle axes of anisotropy:

$$\boldsymbol{\sigma}_n = \begin{bmatrix} \sigma_{n,xx} & 0 \\ 0 & \sigma_{n,yy} \end{bmatrix}, \quad \boldsymbol{\sigma}_p = \begin{bmatrix} \sigma_{p,xx} & 0 \\ 0 & \sigma_{p,yy} \end{bmatrix} \quad (1)$$

$$\mathbf{s}_n = \begin{bmatrix} s_n & 0 \\ 0 & s_n \end{bmatrix}, \quad \mathbf{s}_p = \begin{bmatrix} s_p & 0 \\ 0 & s_p \end{bmatrix},$$

where $s_n < 0$, $s_p > 0$. The total conductivity tensor $\boldsymbol{\Sigma}$ and total resistivity tensor \mathbf{P} are related as $\boldsymbol{\Sigma} = \mathbf{P}^{-1} = \boldsymbol{\sigma}_n + \boldsymbol{\sigma}_p$. The total Seebeck tensor is the weighted sum of the band Seebeck tensors,

$$\mathbf{S} = (\boldsymbol{\sigma}_p + \boldsymbol{\sigma}_n)^{-1}(\boldsymbol{\sigma}_p \mathbf{s}_p + \boldsymbol{\sigma}_n \mathbf{s}_n) \quad (2)$$

Whereas single-band Seebeck tensors \mathbf{s}_n , \mathbf{s}_p are typically isotropic, the conductivity tensors $\boldsymbol{\sigma}_n$, $\boldsymbol{\sigma}_p$ can be strongly anisotropic, and Eq. (2) allows one to exploit this anisotropic conductivity to weight the resulting total Seebeck tensor to opposite signs of Seebeck effect for orthogonal directions. Defining a small parameter ξ as the ambipolar conductivity ratio for a given direction, we shall define the x -direction as dominated by p-type conduction $\xi_x = \sigma_{n,xx} / \sigma_{p,xx} < 1$, and the y -direction by n-type $\xi_y = \sigma_{p,yy} / \sigma_{n,yy} < 1$. The total Seebeck tensor

$$\mathbf{S} = \begin{bmatrix} S_{p,xx} & 0 \\ 0 & S_{n,yy} \end{bmatrix} \quad (3)$$

has the following positive and negative matrix elements, respectively, for small $\xi < s_p s_n / (s_p^2 + s_n^2)$,

$$S_{p,xx} = \frac{s_p + \xi_x s_n}{1 + \xi_x} > 0, \quad (4)$$

$$S_{n,yy} = \frac{s_n + \xi_y s_p}{1 + \xi_y} < 0.$$

To describe the transverse thermoelectric behavior, we define longitudinal and transverse transport axes a and b , respectively. Let the unit vector $\hat{\mathbf{a}} = \cos\theta \hat{\mathbf{x}} + \sin\theta \hat{\mathbf{y}}$ define the direction of current flow $\mathbf{J} = J_a \hat{\mathbf{a}}$ at an angle $+\theta$ relative to the x -axis, with the transverse unit vector $\hat{\mathbf{b}} = -\sin\theta \hat{\mathbf{x}} + \cos\theta \hat{\mathbf{y}}$, as shown in the insert of Fig. 4. The total Peltier heat flux density becomes $\mathbf{Q}_n = \Pi \mathbf{J} = (T \mathbf{S}) \mathbf{J}$ with longitudinal and transverse components,

$$Q_{\Pi,a} = \mathbf{Q}_n \cdot \hat{\mathbf{a}} = (S_{p,xx} \cos^2\theta + S_{n,yy} \sin^2\theta) T J_a \quad (5)$$

$$Q_{\Pi,b} = \mathbf{Q}_n \cdot \hat{\mathbf{b}} = -(S_{p,xx} - S_{n,yy}) \cos\theta \sin\theta T J_a. \quad (6)$$

Note from Eq. (6) that the transverse Peltier effect can be maximized by independently maximizing the magnitude of $S_{p,xx}$ and $S_{n,yy}$.

The total heat flux density $\mathbf{Q} = \mathbf{Q}_n - \boldsymbol{\kappa}^c \nabla T$ will include contributions from both Peltier and thermal conduction effects, where $\boldsymbol{\kappa}^c$ with the explicit superscript c defines the open-circuit

thermal conductivity tensor at $\mathbf{J} = 0$. Assuming $\mathbf{J} = J_a \hat{\mathbf{a}}$ and $\nabla T = \frac{dT}{db} \hat{\mathbf{b}}$, Kooi et al. have shown that the longitudinal electric field component E_a is constant everywhere. Assuming the thermal gradient ∇T is everywhere perpendicular to the heat sink in the $b = 0$ plane, the heat flux component \mathbf{Q}_b depends only on b .

The longitudinal current and transverse heat flow are

$$J_a = \frac{1}{\rho_{aa}} E_a - \frac{S_{ab}}{\rho_{aa}} \frac{dT}{db} \quad (7)$$

$$Q_b = T \frac{S_{ba}}{\rho_{aa}} E_a - (1 + Z_{ba} T) \kappa_{bb}^c \frac{dT}{db}, \quad (8)$$

where the transverse figure of merit is $Z_{ba} T = \frac{S_{ab} S_{ba} T}{\rho_{aa} \kappa_{bb}^c}$.

Under steady state, the current and energy flux densities have zero divergence $\nabla \cdot \mathbf{J} = 0$ and $\nabla \cdot (\mathbf{Q} + \mu \mathbf{J}) = 0$, where μ is the electrochemical potential, and $-\nabla \mu = \mathbf{E}$ defines the electric field. The intuitive result is that Joule heating $E_a J_a$ from the longitudinal current density sources a transverse heat flux density Q_a :

$$\frac{dQ_b}{db} = E_a J_a \quad (9)$$

Equations (7)-(9) define the differential equation:

$$0 = \frac{1}{S_{ab} S_{ba}} E_a^2 - \left[\frac{S_{ab} + S_{ba}}{S_{ab} S_{ba}} + \frac{d \ln(S_{ba} / \rho_{aa})}{d \ln T} \frac{1}{S_{ab}} \right] E_a \frac{dT}{db} + \left[1 + \frac{d \ln(S_{ba} S_{ab} / \rho_{aa})}{d \ln T} + \frac{1}{Z_{ba}} \frac{d \ln \kappa_{bb}^c}{dT} \right] \left(\frac{dT}{db} \right)^2 + \frac{1 + Z_{ba} T}{Z_{ba}} \frac{d^2 T}{db^2} \quad (10)$$

Assuming a limited temperature range with constant thermoelectric coefficients, we get:

$$0 = \left(\frac{E_a}{S_{ab}} - \frac{dT}{db} \right)^2 + \frac{1 + Z_{ba} T}{Z_{ba}} \frac{d^2 T}{db^2} \quad (11)$$

Notice this equation differs from that for the magnetic field-induced Ettingshausen effect, since in that case S_{ab} and S_{ba} have opposite signs and all dT/db terms cancel; whereas in AATT the S_{ab} and S_{ba} are equal, preserving the dT/db term in Eq. (11).

The optimal angle θ_{\perp} which maximizes $Z_{ba} T$ (θ) defines the optimal $Z_{\perp} T$

$$\cos^2 \theta_{\perp} = \frac{1}{1 + \sqrt{\frac{\kappa_{yy} / \kappa_{xx}}{\rho_{yy} / \rho_{xx}}}} \quad (12)$$

$$Z_{\perp} T = Z_{ba}(\theta_{\perp}) T = \frac{(S_{p,xx} - S_{n,yy})^2 T}{(\sqrt{\rho_{xx} \kappa_{xx}} + \sqrt{\rho_{yy} \kappa_{yy}})^2} \quad (13)$$

Note that the angle θ_{\perp} is independent of the Seebeck anisotropy, and approaches $\theta_{\perp} = \pi/4$ as the thermal conductance anisotropy matches the resistance anisotropy $\kappa_{yy}/\kappa_{xx} = \rho_{yy}/\rho_{xx}$. To optimize the electronic band structure it is useful to define a power factor PF_{\perp} from Eq. (13) under the assumption of isotropic $\boldsymbol{\kappa}$ where \mathbf{S} and $\boldsymbol{\rho}$ tensors can be readily calculated with simple scattering assumptions:

$$PF_{\perp} = \frac{(S_{p,xx} - S_{n,yy})^2}{(\sqrt{\rho_{xx}} + \sqrt{\rho_{yy}})^2} \quad (14)$$

II. Experimental determination of thermal conductivity, κ_{yy}

The two different T2SLs studied in this work were grown by molecular beam epitaxy on GaSb substrates. Because this material was designed for p-i-n detectors, it consists of a 0.5 μm GaSb p+ ($\sim 10^{18} \text{ cm}^{-3}$) buffer layer, followed by a 0.5 μm T2SL p+ ($\sim 10^{18} \text{ cm}^{-3}$) region, a 2 μm undoped T2SL layer, a 0.5 μm T2SL n+ ($\sim 10^{18} \text{ cm}^{-3}$) region, and a 10 nm Si doped InAs n+ capping layer. T2SL-1 is composed of 12 monolayers (ML) of InAs and 8 ML of GaSb per period. T2SL-2 is composed of 19 ML of InAs and 18 ML of GaSb per period.

Because of the similarities in composition, the thermal conductivity in this T2SL should be representative of the thermal conductivity in generic T2SL device layers, including the T2SL cladding layers of InAs/AlSb and T2SL active layers of InAs/GaInSb.

Following standard 3ω sample preparation, the thermal conductivity of a sample including the layer of interest is measured relative to a reference sample without the layer. Thus the T2SL is wet-etched away from half the sample with a solution of citric acid and phosphoric acid plus peroxide.

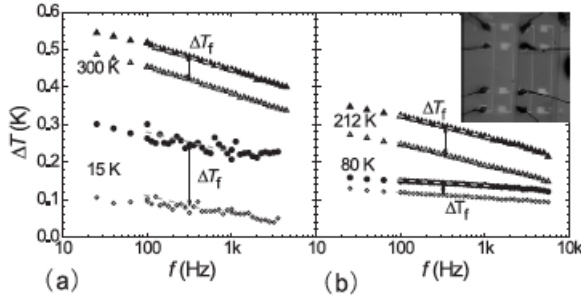


Fig. 1 Temperature change ΔT vs. frequency f measured with the 3ω method for the T2SL + SiO₂ + GaSb substrate (filled symbols) and for SiO₂ + GaSb substrate (open symbols), (a) at 15 K and 300 K, and (b) at 80 K and 212 K. Inset: picture of the sample, with left half etched to substrate, and right half unetched. Two Au heater-thermometer lines are deposited on each side, with current contact pads at top/bottom and voltage contacts in between.

An insulating SiO₂ layer of 150 nm is deposited using plasma enhanced chemical vapor deposition (PECVD) to prevent an electrical short circuit through the conducting substrate. Then 200 nm thick gold heater-thermometer filaments are deposited atop a 3 nm Ti adhesion layer using e-beam evaporation on both etched and unetched regions. The filament shown in the inset of Fig. 1(b) is 3.6 mm long and 30 μm wide, much wider than the 3 μm T2SL thickness so that the heat flow through the T2SL obeys the one-dimensional thermal diffusion equation.

According to the 3ω method,^[5, 6] by sending a current excitation at frequency ω through the gold filament, heating power P is induced at frequency 2ω , leading to thermal variation ΔT at the same frequency and ultimately a 4-point voltage $V_{3\omega}$ at frequency 3ω proportional to the temperature difference via the thermal coefficient of Au. The thermal difference $\Delta T = \Delta T_{\text{sub}}(\omega) + \Delta T_{\text{f}}$ can have a frequency dependent substrate contribution and a frequency independent thin-film contribution,

$$\Delta T_{\text{sub}}(\omega) = \frac{-P}{l\pi\kappa_{\text{sub}}} \frac{1}{2} \ln(2\omega) + C$$

$$\Delta T_{\text{f}} = \frac{P}{\kappa_{\text{f}}} \frac{t}{lw}$$

where κ_{sub} is the thermal conductivity of the GaSb substrate, w and l the width and length of the Au filament heater, and C is a constant offset which includes the SiO_2 layer contribution. For the T2SL film, κ_f and t are the film thermal conductivity and thickness, respectively.

We measured the sample in an Oxford variable temperature insert (VTI) helium gas flow cryostat from 300 K down to 13 K, using standard lock-in techniques. Since there are background 3ω voltages from the lock-in power source and nonlinear components in the measurement circuit and in the lock-in A-B input channels, we also measured a reference background 3ω signal with a low thermal coefficient resistor of equal resistance as the gold filament.

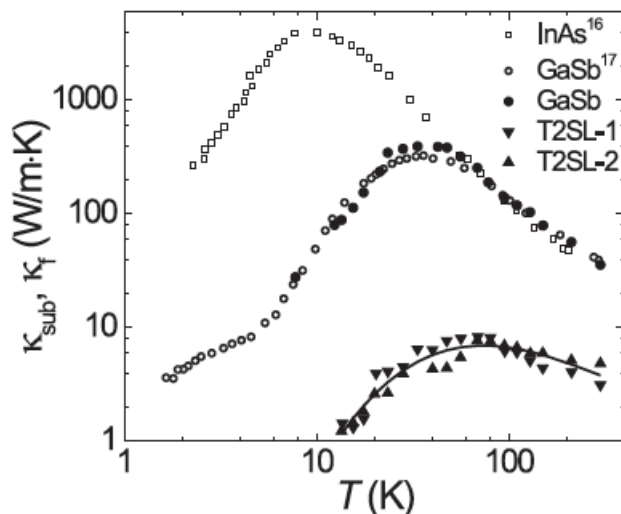


Fig. 2 Cross-plane thermal conductivity for T2SL samples (solid triangles). Measured GaSb substrate thermal conductivity is shown in solid circles. Published data for bulk thermal conductivity of InAs [19] and GaSb [20] are shown for comparison in open squares and open circles respectively. The solid line is a fitting polynomial for the average value of T2SL thermal conductivity described in the text.

By measuring the slope of the temperature difference ΔT as a function of log-frequency, we can deduce the substrate thermal conductivity and thereby confirm the reliability of our measurements. In Fig. 2, we compare our measured GaSb substrate thermal conductivity (solid circles) with previously published GaSb bulk thermal conductivity (open circles)[^{7, 8}], indicating excellent agreement.

The T2SL cross-plane thermal conductivity κ_f is deduced from the thermal difference ΔT_f , plotted with solid triangles in Fig. 2. Previous studies of superlattice thermal conductivities have shown that superlattice thermal conductivity is significantly reduced from those of their constituent bulk materials, resulting from phonon interface scattering, reduced group velocity from modified phonon-dispersion relation, and strain-relaxation induced high density of dislocations [^{9, 10, 11}]. The T2SL value is reduced by 2 orders of magnitude compared with the bulk substrate thermal conductivities for GaSb bulk (open circles). We note that the suppression is much greater, up to as much as $3\frac{1}{2}$ orders of magnitude, when compared with InAs bulk (open squares).

III. Theoretical determination of \mathbf{S} and $\boldsymbol{\rho}$ tensors

Calculations of Seebeck \mathbf{S} and resistivity $\boldsymbol{\rho}$ tensors for the specific case of type II broken-gap InAs/GaSb superlattices (T2SL) are shown to give promising values at room temperature for use as nanoscale transverse thermoelectric refrigerators and generators. Wide-period T2SL's are proposed to be likely candidates for low-temperature cryogenic thermoelectrics.

We can apply the power factor optimization of Eq. (14) to the InAs/GaSb type II broken-gap superlattice (T2SL), and identify it as a likely candidate AATT thermoelectric with its tunable anisotropic electrical conductivity tensor and tunable band gap. The T2SL is a well-studied material for low-dark current infrared detectors and emitters. Because of the broken-gap alignment at the heterointerface, the valence band edge of GaSb lies above the conduction band edge for InAs. Thus by creating superlattices of varying layer width, the quantum confinement

energy can produce a spatially indirect semiconductor with arbitrarily small energy gap. Furthermore, since the heavy hole mass prohibits the holes in GaSb from tunneling through the InAs layers, no hole current flows perpendicular to the superlattice, and the T2SL hole conductivity is maximally anisotropic. One can therefore adopt a 3D ellipsoidal effective mass approximation for the electrons and a 2D circular effective mass approximation for holes to determine the conductivity and Seebeck tensor components:

$$\begin{aligned}
\sigma_{n,xx} &= \frac{2\sqrt{2}e^2\gamma}{3\pi^2\hbar^3} \sqrt{m_{n,y}}(k_B T)^{s+5/2} F_{3/2+s} \left(\frac{E - \mu + E_g}{k_B T} \right) \\
\sigma_{n,yy} &= \frac{2\sqrt{2}e^2\gamma}{3\pi^2\hbar^3} \sqrt{m_{n,x}}(k_B T)^{s+5/2} F_{3/2+s} \left(\frac{E - \mu + E_g}{k_B T} \right) \\
\sigma_{p,xx} &= \frac{e^2\gamma}{\pi d\hbar^2} (k_B T)^{s+2} F_{1+s} \left(\frac{\mu}{k_B T} \right) \\
\sigma_{p,yy} &= 0 \\
s_n &= \frac{-1}{e} [s + 5/2 + (E_g - \mu)/k_B T] \\
s_p &= \frac{+1}{e} [s + 5/2 + \mu/k_B T]
\end{aligned} \tag{15}$$

where m_i represents the effective mass component of the band of interest n or p in the direction of interest x or y , μ is the chemical potential measured relative to the valence band-edge, and F is the Fermi-Dirac integral $F_r(\xi) = \int_0^\infty \xi^r \frac{1}{1+e^\xi}$. The scattering time $\tau = \gamma E^s$ where E is the kinetic energy of the carrier. Since the scattering is dominated by interface scattering, we assume the power factor $s = 0$. Then γ can be calculated from equation $\gamma = \mu_c m^*/e$, where μ_c is the carrier mobility, m^* is the carrier effective mass and e is the electron charge.

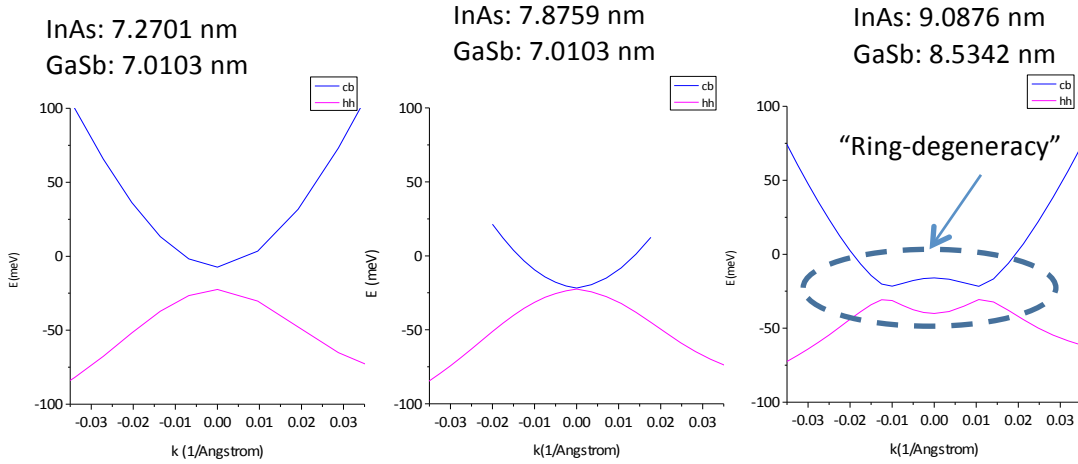


FIG 3. Band simulations of the dispersion relation of a superlattice, show semiconducting behavior (left), zero gap (center), and inverted semimetallic behavior (right). Note the small anticrossing gaps on the right form a highly degenerate ring-shape in momentum space, which functions as a large valley-degeneracy, good for enhancing the Seebeck coefficient at cryogenic temperatures.

These T2SL materials should have an enhanced low-temperature performance in wide-period superlattices. Simulations have been performed on a superlattice structure in Fig. 3, showing that

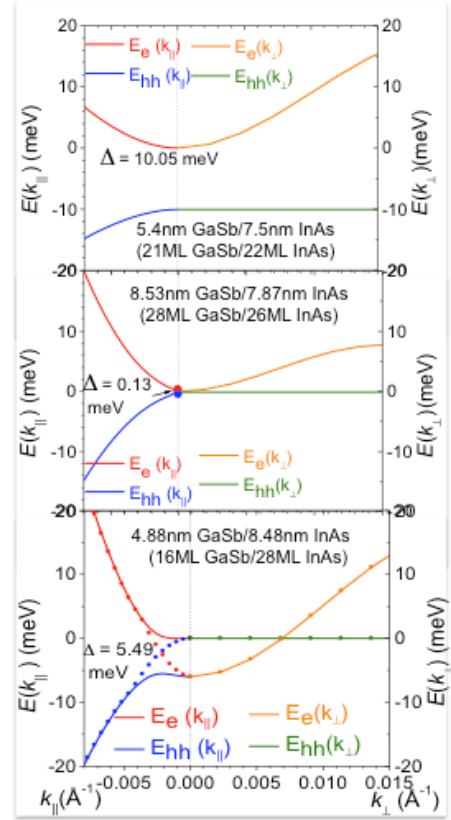
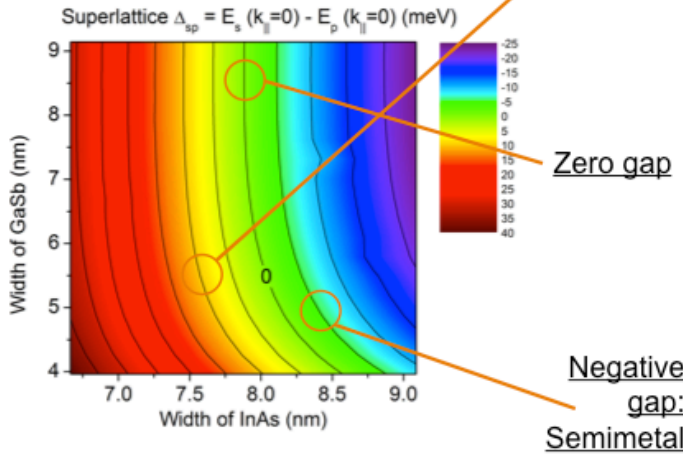
by varying the well thickness it is possible to transition the $k = 0$ band gap from semiconducting, to zero gap, to semimetallic, just as with the double-well case. Note that the small anticrossing gap in the “semimetallic” case will actually result in a large density of states analogous to a valley-degeneracy, and a small gap -- both hallmarks of a good low-temperature thermoelectric material. We propose that this discovery identifies an interesting avenue of future research for cryogenic transverse thermoelectrics.

IV. Optimization of transverse figure of merit $Z_{\perp}T$ and new device geometries

We calculate the band structure of the T2SL with the nextnano3 full-band envelope function method. The figure below shows on the left how the phase space of superlattice layer thickness, d_{GaAs} vs. d_{InAs} is mapped out. Each point in this phase space corresponds to a band structure calculation, as shown on the right. Going from narrow- to wide-periods, one encounters a tunable gap which goes from semiconducting gap to zero gap to semi-metallic. All transport parameters derived the band structure, namely the energy gap and effective masses, are all calculated for every point on the d_{GaAs} vs. d_{InAs} phase space, and the optimal power factor is determined.

Type II Superlattice

NextNANO³: Full-band envelope-function simulation InAs/GaSb superlattice dispersion



Applying the results to Eqs. (14) and Eq. (15), one can maximize the power factor PF_{\perp} at 300 K. The result yields optimal with layer thicknesses $d_{\text{InAs}} = 7.88$ nm and $d_{\text{GaSb}} = 3:96$ nm. The electron and hole effective masses are $m_{n,x} = 0.0303 m_0$, $m_{n,y} = 0.0268 m_0$ and $m_{p,x} = 0.0474 m_0$ where m_0 is the free electron mass. The energy gap is $E_g = 28.3$ meV, and the maximum power factor occurs at chemical potential $\mu = 2.43$ meV. Under the assumption that the thermal conductivity is isotropic, the optimal angle is $\theta_{\perp} = 32^{\circ}$, which means that most of the heat flow will be perpendicular to the superlattice, so the thermal conductivity is dominated by the out-of-plane component experimentally measured in the previous section to be $\kappa = 4$ W/m·K. The

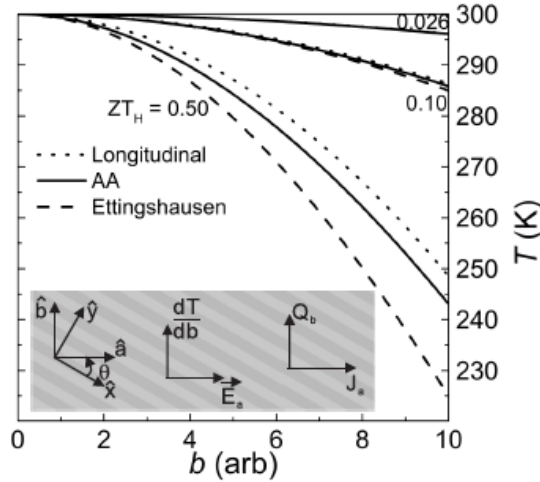


FIG. 4: Temperature profile for Ettingshausen (dashed line), transverse thermoelectric (solid line) and longitudinal thermoelectric (dotted line) cooling for various ZT values. Heat sink is at $b = 0$, $T_H = 300$ K, and $Q_{in}(b = 10\mu\text{m}) = 0$. Electric field is chosen to maximize ΔT . Z is assumed temperature independent, and $S_{ab} = -400 \mu\text{V/K}$.

distinctly different from the Ettingshausen effect for a hypothetical material with the same ZT value (dashed line).

More dramatic improvements in cooling power can be expected for transverse thermoelectrics by exploiting tapered geometries. It has long been known that for longitudinal Peltier coolers, a cascade of ideal lossless thermoelectric junctions with arbitrarily small ZT and multiple stages should cool to arbitrarily low temperatures. The problem with longitudinal thermoelectrics is that the electrical and thermal contact resistance at the interfaces between stages limits the practical implementation to at most 6 stages^{12,13}, and the maximum ΔT is limited

to $\frac{1}{2} ZT_C^2$ for a single stage. In transverse thermoelectrics, since the current and heat flow are perpendicular to each other, infinite cascading can be effectively implemented by making the device exponentially tapered as it approaches the cold load side, as in the insert of

Fig. 5(b). Following the analysis of Kooi et al. for the Ettingshausen effect, this exponential tapering of the device in the perpendicular c -direction adds the term of $Q_b d(\ln c)/db$ to Eq. (9). Assuming exponential tapering $c = c_0 e^{(b/L)}$, where L is the length scale for exponential

optimal ZT is therefore estimated to be $Z_{\perp} T = 0.026$ at room temperature.

The maximum ΔT is reached when the heat load at the cold side is zero. So the boundary conditions for Eq. (11) are $T_H = 300$ K and $Q_{in}(T_C) = 0$. The temperature profile is shown in Fig. 4 for a cross section thickness of $b = 10 \mu\text{m}$ of a superlattice, yielding a total temperature difference $\Delta T_{\text{max}} = 4$ K. We also solve the temperature profile with $ZT_H = 0.1$ or $ZT_H = 0.5$ with the maximum temperature differences of 14 K and 56 K, respectively, and we compare with both longitudinal and Ettingshausen cooling for the same ZT values as shown in Fig. 4. AATT transverse thermoelectric cooling (solid line) is slightly better than the longitudinal thermoelectric cooling (dotted line), and the thermal profile is

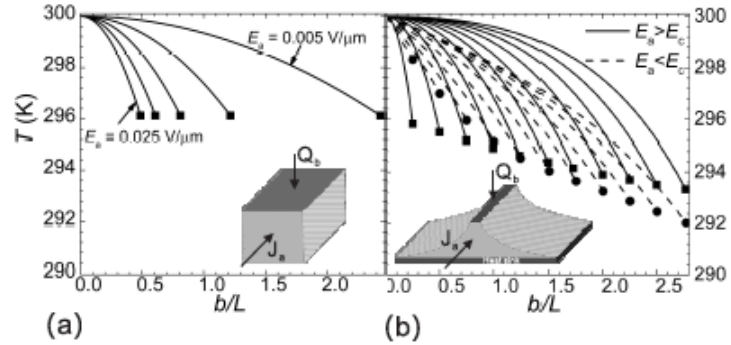


FIG. 5: Temperature profile solved with boundary conditions $T_H(0) = 300$ K, $Q_{in}(T_C) = 0$ at different values of electric field gives the ΔT_{max} at different device thicknesses. The coordinates of the squares and circles identify the minimum T_C for that layer thickness. (a) For the rectangular shape device, the minimum cooling temperature is independent of the layer thickness, but weaker electric fields require thicker layers. The electric fields E_a shown are at step intervals of $0.005 \text{ V}/\mu\text{m}$. (b) For the exponentially tapered device, ΔT_{max} can be arbitrary large with increasing layer thickness.

tapering, Eq. (11) for AATT materials becomes:

$$0 = \left(\frac{E_a}{S_{ab}} - \frac{dT}{db} \right)^2 + \frac{1 + Z_{ba}T}{Z_{ba}} \frac{d^2T}{db^2} - \left(\frac{1 + Z_{ba}T}{Z_{ba}} \frac{dT}{db} - \frac{E_a T}{S_{ab}} \right) / L. \quad (16)$$

Fig. 5 shows the temperature profile solved with different device thicknesses at corresponding values of electric fields for both a rectangular cooler without tapering, and an exponentially tapered device. Note that for the rectangular cooler in Fig. 5(a), the ΔT_{\max} are independent of layer thickness, whereas in Fig. 5(b) the exponential tapering gives an ever ΔT_{\max} with increasing sample thickness. Assuming the same exponential tapering factor as was demonstrated in bismuth semimetals¹⁴ $b = L = 2.77$, the AATT cooling becomes $\Delta T_{\max} = 8$ K. This is competitive with recent experimental results in on-chip cooling by significantly more complex device structures made of superlattice-based longitudinal thin-film thermoelectrics. Solving Eq. (16) for extrema, we find a critical crossover field $E_c = -S_{ab}T_H/L$ for exponentially tapered transverse thermoelectric devices. At $E_a = E_c$, the AATT cooling is balanced with Joule heating at each cross-section perpendicular to \mathbf{b} , and the temperature is uniform in the whole device. $E_a > E_c$ is required for a local maximum in ΔT to exist, wherefore a limit exists for ΔT_{\max} . When $E_a < E_c$, on the other hand, $T(b)$ decreases monotonically and there is no limit for $\Delta T(b)$, which means with a small electric field and a sufficiently thick slab of material, the device can be cooled to arbitrarily low temperature. In reality, the material transport coefficients are temperature dependent, which limits ΔT_{\max} . As shown in Fig. 5(b), for thin devices where $b=L$ is small, ΔT_{\max} are given by $E_a > E_c$ shown with the solid lines. Whereas for thick devices where $b=L$ is large, ΔT_{\max} are given by $E_a < E_c$ shown with the dashed lines.

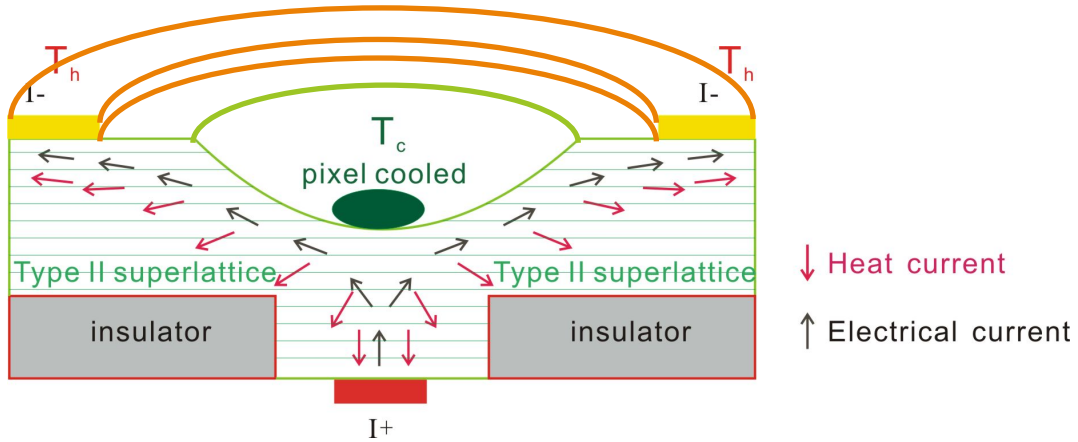


FIGURE of Unconventional transverse thermoelectric cooling geometry. An annular cathode is placed atop a T2SL transverse thermoelectric, fed by a central anode below, surrounding an infrared pixel which is to be cooled. As electrical current (black arrows) flows between the electrodes, the heat current flows opposite the vertical current, but parallel to the lateral current. In between, the transverse thermoelectric effect causes currents at 45 degrees to pull heat away from the central area. At every point, the pixel is being cooled by the electrical current.

IV. Thin-metal-film thermocouple technology

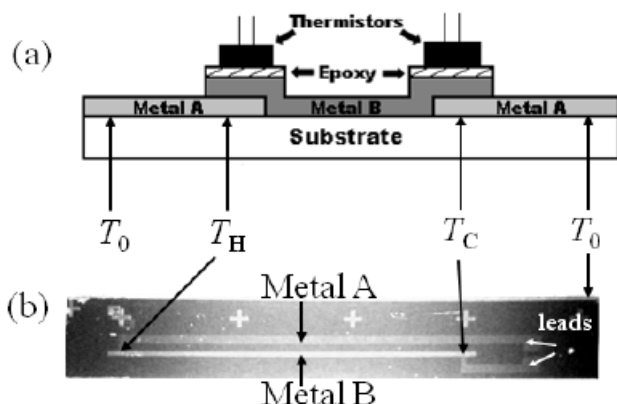


Fig. 6: (a) Conceptual drawing of bimetallic thermocouple layers, where metal A represents the first metal deposited, while metal B represents the second. Heat was applied on backside of substrate behind the hot thermocouple at T_H , whereas the reference cold thermocouple was at T_C . In the real device the left and right leads of Metal A wrap around to form voltage leads. A resistance temperature dependent (RTD) thermistor is epoxied on top of each bimetallic junction calibrating the absolute thermocouple temperatures. (b) Microscope photograph of 50 nm thin film thermocouple of Cr (Metal A) and Ni (Metal B), on a semi-insulating GaAs substrate. Seebeck voltage is measured between leads at T_0 .

Thin film thermocouples are tested for eventual deposition on Type II superlattices. The thermocouples can be placed on the superlattice with an intervening oxide layer for electrical isolation. These thermocouples will calibrate thermal gradients across or along the superlattice so that the Seebeck coefficient and thermal conductivity of the superlattice itself can be calibrated. The best choice for metals was determined to be nickel and chromium, producing a 41 mV/K thermocouple signal. Note that once transverse thermoelectric behavior had been identified, the efforts towards Seebeck and conductivity calibrations were diverted to the thermal conductivity measurements described in Section II, above.

The bimetallic thin-film thermocouples were deposited on blank semiconductor substrates to test their functionality. This newly developed method for measuring temperature gradients can be readily implemented with existing fabrication processes. We first identify specific thin-film metals with a sufficiently large Seebeck coefficient and then demonstrate reproducible process technology on semiconductor substrates. Other impacts of this work include bimetallic thermocouple sensors for integration into microchip fabrication to achieve thermal accuracies within a fraction of a degree Celsius. Samples produced in this research have demonstrated reproducible scaling factors for both inter- and intra-batch, as required for industry applications. Another possible advantage of this technique is that it is entirely passive, allowing in principle for thermal mapping of test samples and microprocessor chips with arbitrary resolution and *zero power overhead*, allowing cryogenic calibrations with no load heating.

The two metals tested here in a thin film thermocouple are chromium Cr and nickel Ni. The thermocouple discussed here is shown in Fig. 6(a), with metal A representing the first metal deposited Cr, and metal B representing the second metal deposited Ni.

The Seebeck effect arises when a temperature difference, $T_H - T_C$, occurs between two junctions of dissimilar conductors. An open-circuit voltage proportional to the junction temperature difference is thereby induced at the leads independent of the lead temperature T_0 ,

$$V_{HC} = \alpha(T_H - T_C) \quad (17)$$

Here V_{HC} represents the Seebeck voltage between the leads. The temperatures T_H and T_C are the temperatures located at the hot and cold thermocouple junctions, respectively, as noted in Fig. 6(b). The temperatures are calibrated with small area (2.0 mm x 3.0 mm) resistance temperature dependent (RTD) thermistors which are epoxied with heat-conducting silver epoxy on top of the metal junctions as shown in Figure 6(a). α is the Seebeck coefficient of the thermocouple. The

bulk Seebeck coefficient α_B expected from literature can be determined by taking the difference of Seebeck coefficients of two dissimilar conductors. Cr and Ni were chosen for their relatively high bulk Seebeck coefficients of +21.8 and -19.5 $\mu\text{V}/^\circ\text{C}$ respectively, to produce a predicted $\alpha_B = 41.3 \mu\text{V}/^\circ\text{C}$. For this study, pure metals were chosen. Though the various alloys of Ni/Cr hold promise for thermocouple applications, alloys are also known to fractionate upon evaporation, possibly making Seebeck calibration less reliable and a topic for future study.

Thermocouple devices, as seen in Fig. 6(b), were fabricated on semi-insulating (SI) GaAs substrate. The GaAs substrate had a thickness of 450 μm and a high bulk resistivity of $3.3 \times 10^6 \Omega\cdot\text{m}$. GaAs was chosen as the semiconductor substrate both for its high resistivity and easy cleaving into narrow strips. Both metal layers were 50 nm thick, made by using positive photoresist photolithography and electron-beam evaporation. To remove any oxide between the two metal layers, an HCl acid dip was performed immediately before the second metal evaporation. The long, narrow thermocouple design in Fig. 6(b) is chosen to provide large linear thermal gradients for a given heater power, allowing for better calibration.

Experiments were conducted by mechanically clamping the cold end of the semiconductor substrate in between two blocks of aluminum, which functioned as a cold sink. Gold wires connected the leads of the device to lines of indium on a glass slide. Copper wires were then connected from the lines of indium on the glass slide to digital multimeters. To simulate an integrated circuit hot spot, a soldering iron was used as the heater element, applied to the backside of the GaAs substrate under the thermocouple. The heater, set at room temperature, was clamped into place to make contact with the back side of the device at the location of T_H as seen in Fig. 6(b). Then the heater power was gradually increased to a desired temperature, and then gradually cooled back down to room temperature. Hysteresis artifacts due to uneven heat flow can thus be identified and avoided. This slow heating process limited the potential adverse effects of rapidly heating the thermocouples which may result in non-linear thermal gradients.

Experimental data was collected for ΔV_{HC} , T_H , and T_C for both increasing and decreasing temperature. Because T_C itself varies with the heat load, any non-linearities in the Seebeck

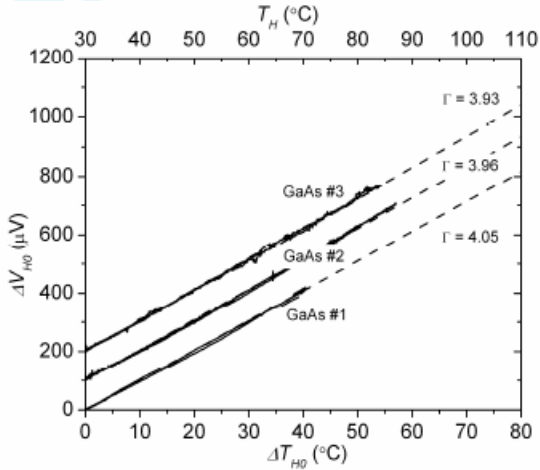


Fig. 7: Parametric plot of thin-film Ni/Cr thermocouple Seebeck response according to Eq. (4), with absolute temperature at the top axis and relative temperature on the bottom axis. Traces are shifted by 100 μV for clarity. Thermocouples were taken from different batches on semi-insulating (SI) GaAs substrates and their Seebeck coefficients were read by the slopes on the voltage vs. temperature plot above. The measured Seebeck coefficients reported in Table 1 was smaller the bulk value by the factor Γ indicated.

response would induce false hysteresis in the thermally cycled raw data. Thus the following relations were used to correct for small thermal variations of T_C :

$$\Delta T_{\text{H0}} = (T_{\text{H}} - T_0) \quad (18)$$

$$\Delta T_{\text{C0}} = (T_{\text{C}} - T_0) \quad (19)$$

$$\Delta V_{\text{H0}} = \Delta V_{\text{HC}} + \frac{dV}{dT} \cdot \Delta T_{\text{C0}} \quad (20)$$

The term ΔV_{H0} represents the Seebeck voltage as a function of ΔT_{H0} while ΔV_{HC} is the Seebeck voltage as a function of ΔT_{HC} determined by (17). The term dV/dT is the linear Seebeck coefficient of the sample for small thermal differences near ambient

temperature, which is calculated by taking the average α_F over the range $\Delta T_{HC} = 0K$ to $\Delta T_{HC} = 20^\circ C$. By implementing these equations, an accurate estimate of the Seebeck response over the full temperature range can be made, without presupposing linearity. ΔT_{H0} and ΔV_{H0} of the devices' responses are plotted in the parametric plots shown in Fig. 2.

The parametric plots of the Seebeck response were observed to be perfectly linear within measurement noise, so that a single Seebeck coefficient α_F of the thin film could be determined from the slope.

$$\alpha_F = \frac{\Delta V_{H0}}{\Delta T_{H0}} \quad (21)$$

Several batches of 50nm GaAs devices were fabricated to determine the design's reproducibility between batches. With ΔT_{H0} representing the absolute temperature change from room temperature and ΔV_{H0} representing the corrected Seebeck voltage, the parametric plots in Fig. 2 exhibit the clear reproducibility of the Seebeck response. The thermocouple range is tested up to $\Delta T_{H0} = 60^\circ C$ equivalent to an absolute temperature of $T_H = 90^\circ C$.

Samples produced thin film Seebeck coefficients α_F smaller than the bulk literature value, so a scaling factor Γ was defined,

$$\Gamma = \frac{\alpha_B}{\alpha_F} \quad (22)$$

The statistics of the devices depicted in Fig. 7 are presented in Table I. The scaling factors for the GaAs #1, GaAs #2 and GaAs #3 samples are quite similar.

The above table describes the important result of this work, namely the reproducible factor of $\Gamma = 3.98$ scaling between the 50 nm thin film Seebeck coefficient and the bulk Seebeck coefficient. The cause of such thin-film reduction of the Seebeck effect has been reported experimentally and investigated theoretically, and is shown to arise when the film thickness is of order or smaller than the electron mean-free-path, such that boundary scattering starts to compete in magnitude with bulk scattering, typically for films thinner than several hundred nanometers, depending on the metal. The difference between the thin film Seebeck coefficient and that of bulk material is inversely proportional to the metal film thickness. Another possible explanation is that the films may incorporate oxygen during deposition resulting in a reduced Seebeck coefficient, though this concern is more relevant for rf sputtered films. Between the two consequent electron-beam evaporations, processing may result in a thin oxide or other process contamination layer which in principle could also reduce the Seebeck coefficient. The likelihood of an oxide layer is reduced since the sample is dipped in HCl acid immediately before the second metal evaporation. However, even if the scaling factor does result from some sort of extrinsic layer, these conditions have been demonstrated here to be reproducible in several attempts. By increasing the thickness of each of the metal layers the Seebeck coefficients could potentially increase closer to the bulk literature value. At higher temperatures up to $700^\circ C$, Moore et al. determined that nonlinearities may enter the Seebeck response of some bulk metals, though the response for the temperatures presented here is demonstrably linear. Thus for a given layer thickness, we have shown that the Seebeck coefficient can be reproducibly calibrated, as we have done here for the 50 nm case. The thermocouples can be scaled down and routed along arbitrarily shaped paths in dedicated metal layers on top of a sample.

TABLE I
REPRODUCIBILITY STATISTICS

Substrate	α_F ($\mu V/^\circ C$)	Γ
GaAs #1	10.19	4.05
GaAs #2	10.43	3.96
GaAs #3	10.50	3.93
Avg	10.37 ± 0.16	3.98 ± 0.06

Conclusion

To conclude, we have introduced the AATT transverse thermoelectrics in semiconductors with anisotropic electron and hole dispersions, whereby longitudinal electrical currents drive transverse heat flow, and deduced the governing transport equations. The phenomenon is shown to be distinctly different from longitudinal thermoelectrics and the Ettingshausen effect. The optimal transverse figure of merit $Z_{\perp}T$ are deduced based on an electron-hole two-band model. The InAs/GaSb T2SL has an appropriate AATT band structure as simulated with the full-band envelope function method. Realistic estimates of the T2SL suggest thermoelectric cooling of 8 K at room temperature, which is competitive with recent results in on-chip cooling by thin-film longitudinal thermoelectrics. Estimates of $Z_{\perp}T = 0.5$ would yield AATT cooling of 56 K at room temperature, and thick, exponentially tapered devices could cool to arbitrarily low temperatures independent of $Z_{\perp}T$ value. We have also established technological capabilities for making thin film thermocouples for the purpose of thermoelectric calibration of T2SL thin films. This work led to 5 published papers, 1 preprint (submitted to PRL) and 2 patent applications.

BIBLIOGRAPHY

-
- ¹ B. J. O'Brien, C. S. Wallace, K. Landecker, *J. Appl. Phys.* **27**, 820 (1956).
 - ² I. Chowdhury, R. Prasher, K. Lofgreen, G. Chrysler, S. Narasimhan, R. Mahajan, D. Koester, R. Alley and R. Venkatasubramanian, *Nature Nanotechnology* **4**, 235 (2009).
 - ³ K. F. Cuff, R. B. Horst, J. L. Weaver, S. R. Hawkins, C. F. Kooi, G. M. Enslow, *Appl. Phys. Lett.* **2**, 145 (1963).
 - ⁴ H. J. Goldsmid, *Introduction to Thermoelectricity*, Chapter 11, Springer-Verlag, ISBN-13: 9783642007163 (2009).
 - ⁵ D. G. Cahill, *Rev. Sci. Instrum.* **61**, 802 (1990); S.-M. Lee and D. G. Cahill, *J. Appl. Phys.* **81**, 2590 (1997).
 - ⁶ D. G. Cahill, M. Katiyar, and J. R. Abelson, *Phys. Rev. B* **50**, 6077 (1994).
 - ⁷ P. V. Tamarin and S. S. Shalyt, *Sov. Phys. Semicond.* **5**, 1097-1098 (1971)
 - ⁸ M. G. Holland, *Phys. Rev.* **134**, A471 (1964).
 - ⁹ W. S. Capinski, H. J. Maris, T. Ruf, M. Cardona, K. Ploog, D. S. Katzer, *Phys. Rev. B* **59**, 8105 (1999).
 - ¹⁰ G. Chen, *Phys. Rev. B* **57**, 14 958 (1998).
 - ¹¹ S.-M. Lee, David G. Cahill, *Appl. Phys. Lett.*, **70**, 2957 (1997).
 - ¹² V. A. Semenyuk, D. M. Rowe, ed, *Thermoelectrics Handbook: Macro to Nano*, Chapter 17, CRC Press, (2006).
 - ¹³ H. J. Goldsmid, D. M. Rowe, ed, *Thermoelectrics Handbook: Macro to Nano*, Chapter 3, CRC Press, (1995).
 - ¹⁴ K. Scholz, P. Jandl, U. Birkholz, Z. M. Dashevskii, *J. Appl. Phys.*, **75**, 5407 (1994).